# Electromagnetic Characteristics Analysis and Optimization for Magnetic-Axis-Offset Hybrid-Pole Interior Permanent Magnet Motor

Haoyang Xu, Liwei Shi, Ziheng Pan, Ruohe Rong, and Shifeng Shi

Abstract—To reduce reliance on rare-earth permanent magnet materials while enhancing torque output capability, this paper proposes a Magnetic-Axis-Offset Hybrid-Pole Interior Permanent Magnet Motor (MAOHP-IPMM). The motor features an asymmetric magnetic barrier geometry combined with biased hybrid poles, which induces a Magnetic Axis Offset (MAO) effect. This configuration shifts the permanent magnet flux linkage, thereby reducing the current phase difference between the peak permanent magnet torque and reluctance torque. Firstly, the topology and torqueenhancement mechanism of the MAOHP-IPMM are elaborated. A mathematical model is then derived from the power balance equation, incorporating the magnetic axis offset angle to quantify the MAO effect. Subsequently, a hierarchical optimization strategy is adopted, integrating the Box-Behnken Design (BBD) response surface methodology and multiobjective genetic algorithm (MOGA-II) to perform multiobjective optimization of critical design parameters. Finite element simulations show that, compared to the conventional interior permanent magnet motor (TIPMM), the MAOHP-IPMM increases average torque by 5.5% while reducing NdFeB magnet consumption by 15.6%, confirming its significant torque enhancement. Experimental validation via prototype testing verifies both the MAO effect and the torque enhancement capability of the MAOHP-IPMM.

Index Terms—Interior permanent magnet motor, asymmetric rotor, hybrid pole, magnetic-axis-offset effect, reluctance torque

## I. INTRODUCTION

PERMANENT magnet synchronous motors (PMSMs) are widely used as drive motors for new energy vehicles due to their advantages of high efficiency, high power density, wide speed range and high reliability[1-4]. According to the different placement of permanent magnets, PMSM can be divided into two categories: surface permanent magnet motors (SPMMs) and interior permanent magnet motors

Manuscript received May 23, 2025; revised September 26, 2025.

This work was supported by the Natural Science Foundation of Shandong Province, China, under Grant ZR2024ME089 and National Natural Science Foundation of China under Grant 51975340.

Haoyang Xu is a postgraduate student at the School of Transportation and Vehicle Engineering, Shandong University of Technology, Zibo 255049, China (e-mail: 1913745578@qq.com).

Liwei Shi is a professor, doctoral supervisor of Shandong Key Laboratory of Integrated Design and Intelligence of New Energy Vehicles, Zibo 255000, China (corresponding author; e-mail: shiliwei@sdut.edu.cn).

Ziheng Pan is a postgraduate student at Shandong University of Technology, Zibo 255049, China (e-mail: 283641854@qq.com).

Ruohe Rong is a postgraduate student at Shandong University of Technology, Zibo 255049, China (e-mail: eulerrh@163.com).

Shifeng Shi is a postgraduate student at Shandong University of Technology, Zibo 255049, China (e-mail: 15922845706@163.com).

(IPMMs). The former places the permanent magnets on the rotor surface, while the latter embeds them within the rotor core [5-7]. Since the reluctance of permanent magnets is similar to that of air, the inductance of the dq-axis in SPMM is almost equal, resulting in no reluctance torque [8]. In contrast, the special rotor structure and permanent magnet arrangement of IPMM creates a difference between the dq-axis inductance ( $L_q$ - $L_d$ ), which results in two torque components: permanent magnet torque and reluctance torque. This significantly improves the motor torque density [9-10].

However, for traditional interior permanent magnet motors (TIPMM), the phase angles corresponding to the peak values of permanent magnet torque and reluctance torque differ by 45° [11]. Consequently, the maximum total output torque is not a simple superposition of the individual peak torques due to the sinusoidal nature of the torque-current angle curves. This results in relatively low utilization rates for both torque components. Additionally, the rising prices of rare-earth permanent magnet materials have led to increased attention toward rare-earth-reduced or rare-earth-free motors [12-13]. Therefore, enhancing torque output while using less rare-earth PM material and improving torque utilization has become an important research focus.

In recent years, in response to the above problems, numerous scholars have proposed the use of asymmetric rotor structure to reduce the current phase angle difference between the maximum permanent magnet torque and the reluctance torque component, aiming to improve the total output torque without increasing the amount of rare-earth permanent magnet materials. The specific structural schemes adopted mainly include the axial hybrid rotor [14-15], permanent magnet asymmetry [16-17], rotor core asymmetry [18] and so on. For example, literature [19] studied an axial hybrid rotor motor, in which the rotor is divided into two structures: interior permanent magnet and synchronous reluctance in the axial direction. The total torque is improved by changing the tangential displacement angle of the two rotor segments so that the permanent magnet torque and the reluctance torque reach their maximum value at the same current angle, and prototypes were fabricated for validation. However, its unique rotor structure also leads to a complicated fabrication process and results in certain axial magnetic leakage at the segments. Literature [20] proposed a new type of asymmetric pole motor with a symmetric rotor core structure, and the total torque is improved by means of the asymmetric arrangement of the permanent magnets, causing the d-axis of the permanent magnets to shift, but the effect is not significant. Literature [21] and [22] investigated a structure with symmetric permanent magnet but an asymmetric rotor core, and the solutions such as radial asymmetric spoke-type magnetic barriers and nonuniform air-gap are used to make the reluctance axis shift and thereby reduce the current phase angle difference between the maximum permanent magnet torque and the reluctance torque. However, the reluctance axis shift further increases the difficulty of control.

Based on existing studies, it can be found that the torque enhancement effect is often directly proportional to the degree of magnetic axis offset, but problems such as waveform distortion and torque ripple increase as the magnetic axis offset intensifies. Therefore, it is essential to make trade-offs in the motor design process instead of pursuing torque improvement blindly. Furthermore, rare-earth permanent magnet materials remain predominantly used for excitation in current research, which does not facilitate reducing dependence on rare-earth resources.

Therefore, this paper proposes a novel magnetic-axisoffset hybrid-pole interior permanent magnet motor (MAOHP-IPMM). Through an asymmetric magnetic barrier combined with a unique pole arrangement, the magnetic axis offset (MAO) effect is generated, reducing the current angle difference between the peak permanent magnet torque and reluctance torque. This approach achieves torque enhancement while reducing rare-earth permanent magnet consumption. Section II introduces the motor structure and develops its mathematical model, followed by multiobjective optimization. Section III analyzes electromagnetic characteristics of the MAOHP-IPMM in comparison with a traditional interior permanent magnet motor (TIPMM). Finally, a prototype was fabricated and an experimental platform was established to verify the MAO effect.

#### II. STRUCTURAL DESIGN AND MATHEMATICAL MODEL

## A. Motor topology and basic parameters

The topologies of the TIPMM and the proposed MAOHP-IPMM are shown in Fig. 1. Both motors adopt 48slot/8-pole distributed windings and share an identical stator structure. The TIPMM employs a combined V-type and tangential single-bar pole arrangement with pure NdFeB excitation, where both the permanent magnet arrangement and magnetic barrier structure are fully symmetrical. In contrast, the MAOHP-IPMM utilizes hybrid poles composed of low-cost Ferrite and high-performance NdFeB. Its magnetic barrier structure exhibits intentional asymmetry in three aspects: barrier angle, spatial interval, and geometric shape. Furthermore, the permanent magnet arrangement is deliberately asymmetric: Ferrite magnets are placed on the left side of the V-shaped magnetic barrier, while NdFeB magnets occupy the right side, and an additional NdFeB magnet is tangentially placed outside the arc-shaped magnetic barrier.

Compared with the TIPMM, the MAOHP-IPMM employs a slightly asymmetric magnetic barrier, hybrid poles, and tangential permanent magnet biasing to guide permanent magnet flux offset. This configuration reduces the current angle difference between the peak permanent

magnet torque and reluctance torque components, consequently enhancing the motor's output torque. This phenomenon is defined as the magnetic-axis-offset (MAO) effect in this paper.

The key design parameters for both motors are listed in Table I.

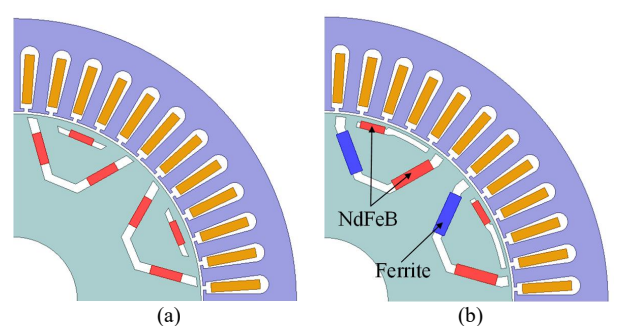


Fig. 1. Rotor topology. (a) TIPMM. (b) MAOHP-IPMM.

TABLE I MAIN DESIGN PARAMETERS OF THE TWO MOTORS

Parameters	TIPMM	MAOHP-IPMM
Rated power	7 kW	7 kW
Rated voltage	72 V	72 V
Rated speed	3000 r/min	3000 r/min
Stator inner diameter	107.4 mm	107.4 mm
Stator outer diameter	160 mm	160 mm
Rotor inner diameter	36 mm	36 mm
Rotor outer diameter	106 mm	106 mm
PM materials	NdFeB	Ferrio/NdFeB

#### B. Mathematical model of the motor

Before establishing the mathematical model of the motor, the following assumptions are adopted:

- 1)Neglect magnetic saturation, as well as eddy current and hysteresis loss in the motor.
- 2)Neglect the magnetic reluctance of the stator and rotor cores.
- 3)Assume ideal sinusoidal waveforms for voltage, current, and back-EMF.

For traditional permanent magnet motors, the direction aligned with the N pole of the permanent magnet is conventionally defined as the motor's d-axis. the counterclockwise direction is designated as the positive rotational direction, while the axis leading the d-axis by 90° electrical angle in the rotational direction constitutes the qaxis. Due to the TIPMM's symmetrical structure, its permanent magnet flux linkage remains coaxial with the daxis. On the basis of the TIPMM, the proposed MAOHP-IPMM incorporates permanent magnet offset and structural modifications. This causes the permanent magnet flux linkage to deflect toward the rotational direction, introducing the magnetic axis offset angle γ. To model this effect, an equivalent replacement of rotor-slot permanent magnets with excitation windings is implemented, establishing the equivalent physical model shown in Fig. 2. Based on Blondel's double-reaction theory, Fig. 3 depicts the steady-state vector diagrams of both motors in the d-qsynchronous rotating coordinate system. Fig. 3(a) illustrates the steady-state vector diagram of the TIPMM, while Fig. 3(b) shows the MAOHP-IPMM's diagram. Since the back-EMF e<sub>0</sub> generated by the permanent magnet flux linkage leads the flux linkage by 90° electrical angle, it is evident from Fig. 3(b) that  $e_0$  also shifts by angle  $\gamma$ . Consequently, the voltage and flux linkage equations of the MAOHP-IPMM differ significantly from those of the TIPMM, resulting in corresponding differences in their torque equations.

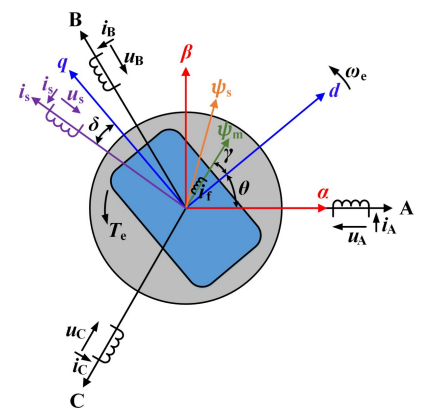


Fig. 2. Equivalent physical model of MAOHP-IPMM.

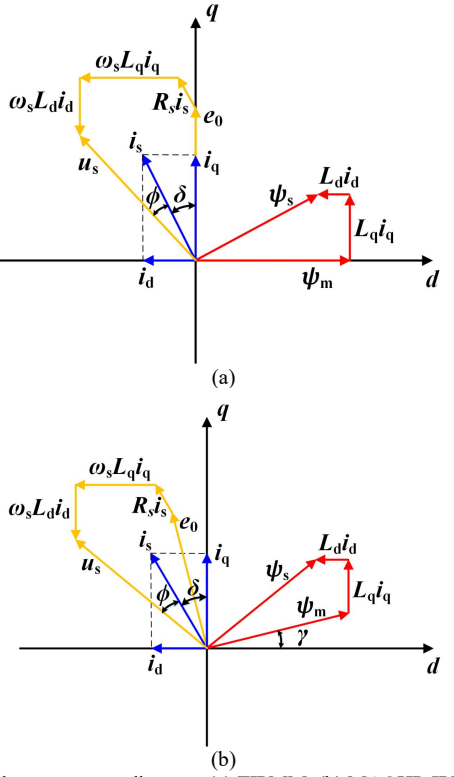


Fig. 3. Steady-state vector diagram. (a) TIPMM. (b) MAOHP-IPMM.

According to the MAOHP-IPMM equivalent physical model and the steady-state vector diagrams of the two motors, the dq-axis stator voltage equation of the motor can be obtained

$$\begin{cases} u_d = R_s i_d + \frac{d}{dt} \psi_d - \omega_e \psi_q \\ u_q = R_s i_q + \frac{d}{dt} \psi_q + \omega_e \psi_d \end{cases}$$
 (1)

where  $u_d$  and  $u_q$  are the d-axis and q-axis components of the stator voltage,  $R_s$  is the armature resistance,  $i_d$  and  $i_q$  are the d-axis and q-axis components of the stator current,  $\psi_d$  and  $\psi_q$  are the d-axis and q-axis components of the flux linkage, and  $\omega_e$  is the rotor electrical angular velocity.

According to Fig. 3(a), the dq-axis flux linkage equation can be expressed as

$$\begin{cases} \psi_d = L_d i_d + \psi_m \\ \psi_q = L_q i_q \end{cases}$$
 (2)

where  $L_d$  and  $L_q$  are the *d*-axis and *q*-axis inductance, respectively, and  $\psi_m$  is the permanent magnet flux linkage.

According to Fig. 3(b), the dq-axis flux linkage equation of MAOHP-IPMM can be obtained by introducing the magnetic axis offset angle  $\gamma$ 

$$\begin{cases} \psi_d = L_d i_d + \psi_m \cos \gamma \\ \psi_q = L_q i_q + \psi_m \sin \gamma \end{cases}$$
 (3)

Substituting Eq. (3) into Eq. (1) yields the *dq*-axis stator voltage equation for the MAOHP-IPMM

$$\begin{cases} u_d = R_s i_d + \frac{d}{dt} (L_d i_d + \psi_m \cos \gamma) - \omega_e (L_q i_q + \psi_m \sin \gamma) \\ u_q = R_s i_q + \frac{d}{dt} (L_q i_q + \psi_m \sin \gamma) + \omega_e (L_d i_d + \psi_m \cos \gamma) \end{cases}$$
(4)

In the above equation, the middle term is the derivative of the flux linkage with respect to time, and the result is 0, so the above equation can be further simplified as

$$\begin{cases} u_d = R_s i_d - \omega_e L_q i_q - \omega_e \psi_m \sin \gamma \\ u_q = R_s i_q + \omega_e L_d i_d + \omega_e \psi_m \cos \gamma \end{cases}$$
 (5)

Combining the analysis of Fig. 2 and the preceding equations, it is evident that the magnetic axis offset angle  $\gamma$  directly impacts the permanent magnet flux linkage, thereby influencing the d-axis and q-axis stator voltage components. Subsequently, the torque equation of the MAOHP-IPMM will be derived based on power balance principles.

In the ABC three-phase natural coordinate system, the input power of the motor is

$$P_0 = u_a i_a + u_b i_b + u_c i_c (6)$$

where  $P_0$  is the motor input power,  $u_a$ ,  $u_b$  and  $u_c$  are the three-phase armature winding voltage,  $i_a$ ,  $i_b$  and  $i_c$  are the three-phase armature winding current respectively.

The Clark and Park transforms are applied to the above equation to obtain the input power equation in the dq-axis synchronized rotation coordinate system

$$P_0 = \frac{3}{2} (u_d i_d + u_q i_q) \tag{7}$$

According to the assumptions, the following equation can be obtained

$$P = P_0 \tag{8}$$

where P is the motor output power.

Thus, the output power equation of the moter can be obtained

$$P = \frac{3}{2} (u_d i_d + u_q i_q)$$

$$= \frac{3}{2} [(R_s i_d - \omega_e L_q i_q - \omega_e \psi_m \sin \gamma) i_d +$$

$$(R_s i_q + \omega_e L_d i_d + \omega_e \psi_m \cos \gamma) i_q]$$

$$= \frac{3}{2} [\omega_e \psi_m (i_q \cos \gamma - i_d \sin \gamma) + (L_d - L_q) \omega_e i_d i_q]$$
(9)

The relationship between the mechanical angular velocity and the electrical angular velocity of the motor is as follows

$$\omega = \frac{\omega_e}{p_n} \tag{10}$$

where  $\omega$  is the mechanical angular velocity of the motor, and  $p_n$  is the number of motor pole pairs.

Therefore, the output torque of the motor equals the output power divided by the mechanical angular speed

$$T_{e} = \frac{P}{\omega} = \frac{p_{n}P}{\omega_{e}}$$

$$= \frac{3}{2} p_{n} \left[ \psi_{m} (i_{q} \cos \gamma - i_{d} \sin \gamma) + (L_{d} - L_{q}) i_{d} i_{q} \right]$$
(11)

The stator current components  $i_d$  and  $i_q$  in the dq-axis synchronous rotation coordinate system are expressed as follows

$$\begin{cases} i_d = -i_s \sin \delta \\ i_q = i_s \cos \delta \end{cases}$$
 (12)

where  $i_s$  is the stator current vector, and  $\delta$  is the current phase angle.

Bringing Eq. (12) into Eq. (11), the MAOHP-IPMM torque equation considering the magnetic axis offset angle  $\gamma$  can be obtained

$$T_{e} = \frac{3}{2} p_{n} [\psi_{m} (i_{s} \cos \delta \cos \gamma + i_{s} \sin \delta \sin \gamma) - (L_{d} - L_{q}) i_{s}^{2} \sin \delta \cos \delta]$$

$$= \frac{3}{2} p_{n} \left[ \psi_{m} i_{s} \cos(\delta - \gamma) + \frac{1}{2} i_{s}^{2} (L_{q} - L_{d}) \sin 2\delta \right]$$
(13)

Rearranging the above equation derives the permanent magnet torque and reluctance torque expressions for the MAOHP-IPMM as follows

$$\begin{cases}
T_{pm} = \frac{3}{2} p_n \psi_m i_s \cos(\delta - \gamma) \\
T_r = \frac{3}{4} p_n i_s^2 (L_q - L_d) \sin 2\delta
\end{cases} \tag{14}$$

It can be found that when the current phase angle  $\delta$  takes a constant value and satisfies the condition of  $\delta$ - $\gamma$ >0, the permanent magnet torque  $T_{\rm pm}$  increases with the magnetic axis offset angle  $\gamma$  because  $\cos(\delta$ - $\gamma)$  increases. Meanwhile, the reluctance torque  $T_{\rm r}$  remains unchanged, resulting in an increase in total torque. This theoretically explains how magnetic axis offset enhances output torque.

## III. MULTI-OBJECTIVE OPTIMIZATION

To further enhance the output performance of the proposed motor while maintaining the MAO effect, multiparameter optimization is required due to complex parameter interactions. Traditional single-objective optimization cannot meet this demand, necessitating multiobjective optimization. For electric vehicle drive motors requiring large-torque output, while considering operational stability and ride comfort, this study selects both output torque and torque ripple as optimization objectives. The specific optimization process is illustrated in Fig. 4.

Firstly, based on the motor structure and mathematical model, the optimization variables and constraints are defined, and the motor parametric model is established. Subsequently, single-parameter scanning of the optimization variables is performed to determine their value ranges. Then, comprehensive sensitivity analysis of the optimization variables is conducted, yielding two variable groups: high

sensitivity and low sensitivity. Finally, both groups are optimized separately using the multi-objective genetic algorithm and response surface method, respectively, with final optimization results outputted.

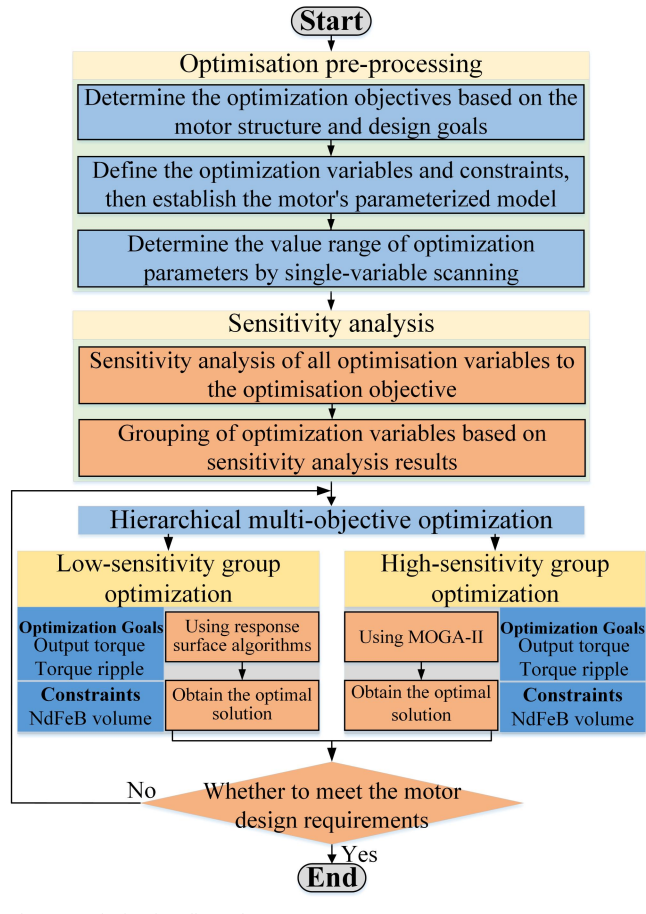


Fig. 4. Optimization flow chart.

## A. Optimization pre-processing

The proposed MAOHP-IPMM incorporates two torque components, the permanent magnet torque and reluctance torque, necessitating comprehensive consideration of optimization parameter selection. The shape, position, and angle of the magnetic barrier significantly impact reluctance torque and substantially influence motor torque ripple, while the size and position of permanent magnets primarily affect permanent magnet torque. Furthermore, during optimization, the optimal current angle varies with changes in the position and shape of both magnetic barriers and permanent magnets, thereby altering the magnetic axis offset angle  $\gamma$ .

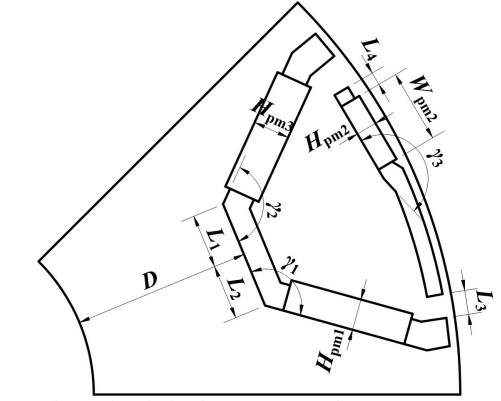


Fig. 5. Topology of optimization parameters for MAOHP-IPMM.

Consequently, the current angle must be included as an optimization variable. Based on the above analysis, the optimization variables are finalized, and their value ranges determined via single-variable scanning. The topology of these optimization parameters is illustrated in Fig. 5, with specific variables and value ranges summarized in Table II.

TABLE II
OPTIMIZATION PARAMETERS AND VALUE RANGE

Of THIRD THE WIETERS THE VIEWE RETAINED		
Optimization variable	Value range	
Distance from bottom of magnetic barrier to inner circle of rotor D	[15mm,19mm]	
Middle magnetic barrier left length $L_1$	[5mm,7mm]	
Middle magnetic barrier right side length $L_2$	[5mm,8mm]	
Width of the bridge at the right end of the arc magnetic barrier $L_3$	[1.5mm,3mm]	
Outer NdFeb left end magnetic barrier width $L_4$	[0mm,1mm]	
Left NdFeB thickness $H_{pml}$	[2.5mm,3mm]	
Outer NdFeB thickness $H_{pm2}$	[1.8mm,2.2mm]	
Right Ferrite thickness $H_{pm3}$	[3mm,4mm]	
Outer NdFeB width $W_{pm2}$	[7mm,9mm]	
Right magnetic barrier angle $\gamma_1$	[125°,135°]	
Left magnetic barrier angle $\gamma_2$	[130°,140°]	
Outside NdFeB deflection angle $\gamma_3$	[166°,180°]	

## B. Comprehensive sensitivity analysis

Since each optimization parameter exhibits varying degrees of influence on the objective, comprehensive sensitivity analysis of the variables is performed based on the preceding analysis. By introducing a comprehensive sensitivity function, the influence factor of each variable on the optimization objective is quantified, enabling the grouping of optimization variables into high-sensitivity and low-sensitivity categories.

The effect of a single optimization parameter on the optimization objective can be expressed by the sensitivity index, which is calculated as follows

$$G(x_i) = \frac{Var(E(y_i \mid x_i))}{Var(y_i)}$$
 (15)

where  $x_i$  denotes the selected optimization parameters,  $y_i$  denotes the corresponding optimization objective,  $E(y_i|x_i)$  denotes the average value of  $y_i$  with respect to  $x_i$ ,  $Var(E(y_i|x_i))$  and  $Var(y_i)$  denote the variance of  $E(y_i|x_i)$  and  $y_i$ , respectively.

The value of sensitivity index  $G(x_i)$  reflects the sensitivity of the optimization objective to the parameters, The greater the absolute value of  $G(x_i)$ , the stronger the influence of the parameters on the objectives. Based on the sensitivity index calculations, the radar diagram in Fig. 6 illustrates the sensitivity of the optimization variables to different objectives. Fig. 6 indicates that parameters  $L_2$ , D,  $\gamma_3$ ,  $\gamma_1$ , and  $W_{pm2}$  significantly influence output torque, while  $\gamma_1$ ,  $\gamma_3$ ,  $L_3$ , and  $L_2$  exert greater effects on torque ripple.

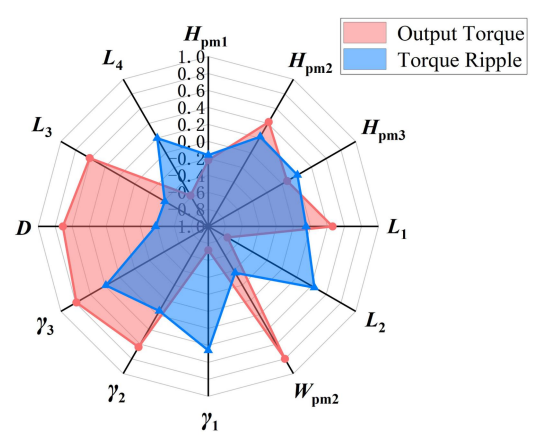


Fig. 6. Sensitivity analysis result.

While the aforementioned sensitivity analysis results characterize the impact of optimization variables on individual objectives, they cannot capture their aggregate effects. To address this limitation, a comprehensive sensitivity function is defined to quantify the holistic influence of optimization variables across all objectives

$$H(x_i) = \mu_{avg} |G_{avg}(x_i)| + \mu_{rip} |G_{rip}(x_i)|$$
 (16)

where  $\mu_{\rm avg}$  and  $\mu_{\rm rip}$  denote the weight coefficients for output torque and torque ripple, respectively, and  $|G_{\rm avg}(x_{\rm i})|$  and  $|G_{\rm rip}(x_{\rm i})|$  represent the absolute sensitivity values of each optimization variable to output torque and torque ripple. Given that electric vehicle drive motors require high output torque while demanding stringent vibration and noise performance, both weight coefficients are assigned a value of 0.5 in this study.

Comprehensive sensitivity analysis is performed using Eq. (16), yielding two variable groups: high-sensitivity and low-sensitivity. The groupings are detailed in Table III.

TABLE III
COMPREHENSIVE SENSITIVITY GROUPING RESULTS

COM RELEASIVE SENSITIVITY GROCI IN GRESCETS		
Group	Optimization variables	
Low sensitivity group	$H_{\rm pm1}, H_{\rm pm2}, H_{\rm pm3}, L_1, L_4, \gamma_2$	
High sensitivity group	$W_{\text{pm2}}, L_2, L_3, \gamma_1, \gamma_3, D$	

#### C. Hierarchical multi-objective optimization

Based on the results of comprehensive sensitivity grouping, the low-sensitivity group and high-sensitivity group are optimized separately using different methods.

The low-sensitivity group exhibits significant interactions among optimization variables and differential influences on each objective. Consequently, the response surface method (RSM) is employed to optimize these variables. The Box-Behnken Design (BBD) method designs experimental plans for variables and objectives, generating an orthogonal sample matrix. Finite element simulation analyzes the resulting parameter combinations to acquire experimental data. Quadratic regression equations are then derived from these data, fitting the functional relationships between variables and targets as follows

$$F(x) = k_0 + \sum_{i=1}^{n} k_i x_i + \sum_{i=1}^{n} k_{ii} x_i^2 + \sum_{i=1}^{n} \sum_{i < j}^{n} k_{ij} x_i x_j + \varepsilon$$
 (17)

where F(x) denotes the response value of different design points,  $k_0$ ,  $k_i$ ,  $k_{ii}$  and  $k_{ij}$  are the fitting coefficients for optimization variables,  $x_i$  and  $x_j$  represent two distinct

optimization variables, n is the number of optimization variables, and  $\varepsilon$  is the fitting error.

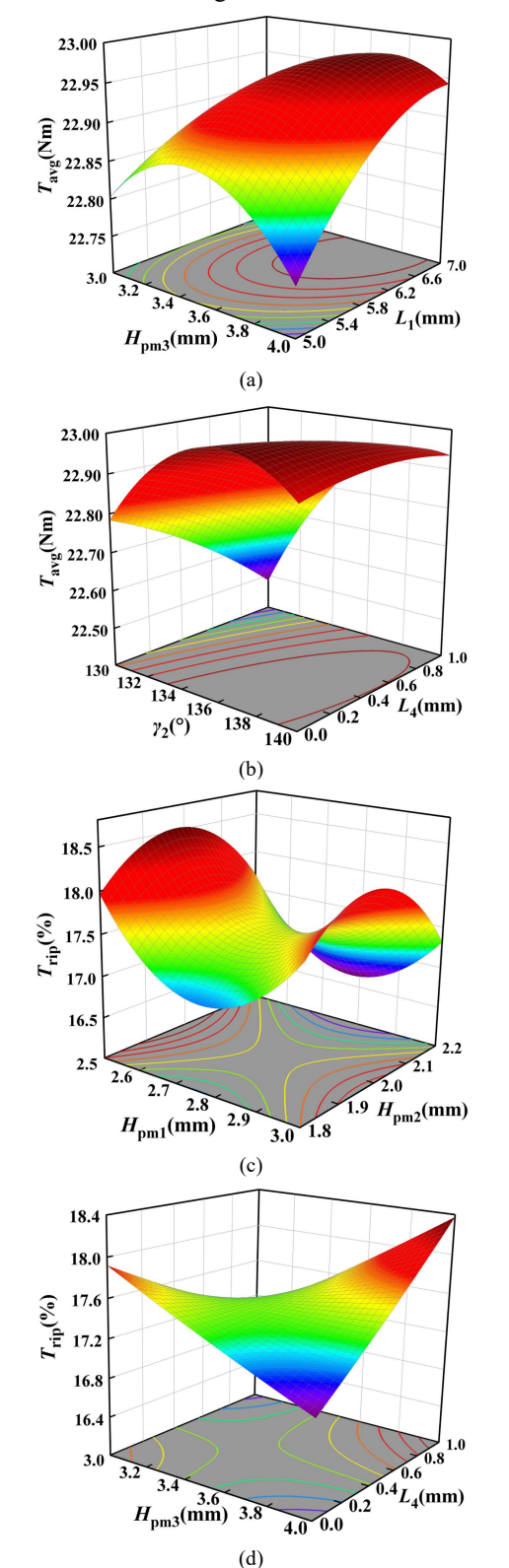


Fig. 7. Response surfaces of some low sensitivity parameters to  $T_{\text{avg}}$  and  $T_{\text{rip}}$ .

According to the fitting equation, response surfaces of  $H_{\rm pm1}$ ,  $H_{\rm pm2}$ ,  $H_{\rm pm3}$ ,  $L_{\rm 1}$ ,  $L_{\rm 4}$ , and  $\gamma_{\rm 2}$  for average torque ( $T_{\rm avg}$ ) and torque ripple ( $T_{\rm rip}$ ) can be established. Fig. 7 shows response surfaces of representative partial optimization parameters. Fig. 7(a) displays the interaction of  $H_{\rm pm3}$  and  $L_{\rm 1}$  on  $T_{\rm avg}$ , within the variable ranges,  $T_{\rm avg}$  increases then decreases with the increase of  $H_{\rm pm3}$ , and rapidly increases then slightly decreases with increasing  $L_{\rm 1}$ . Contour line density indicates

 $H_{\rm pm3}$  dominates  $L_1$  in influence magnitude on  $T_{\rm avg}$ . Fig. 7(b) shows the interaction of  $\gamma_2$  and  $L_4$  on  $T_{\rm avg}$ ,  $T_{\rm avg}$  increases and then decreases with  $\gamma_2$  growth while decreasing overall with  $L_4$  increase. The influence of  $\gamma_2$  on  $T_{\rm avg}$  is stronger than  $L_4$ . Fig. 7(c) illustrates  $H_{\rm pm1}$  and  $H_{\rm pm2}$  interacting on  $T_{\rm rip}$ .  $T_{\rm rip}$  first decreases and then increases with  $H_{\rm pm1}$  rise, whereas it increases then decreases with  $H_{\rm pm2}$  growth. Both parameters show comparable influence. Fig. 7(d) demonstrates  $H_{\rm pm3}$  and  $L_4$  interacting on  $T_{\rm rip}$ , revealing strong coupling that complicates the characterization of variation patterns.

The high-sensitivity group optimization variables are optimized using the Multi-Objective Genetic Algorithm MOGA-II. To comply with the rare-earth-minimization principle, the NdFeB permanent magnet volume is constrained. Additionally, the current phase angle is incorporated as a dynamic optimization variable to adapt to its variation during the process. The constraints are defined as follows

$$V_{\text{NdFeB}} \le 36400 \text{mm}^3 \tag{18}$$

After continuous iteration, the optimization process converges to a well-defined Pareto frontier, as shown in Fig. 8. An optimal design point is identified on this frontier, balancing the trade-offs between competing objectives.

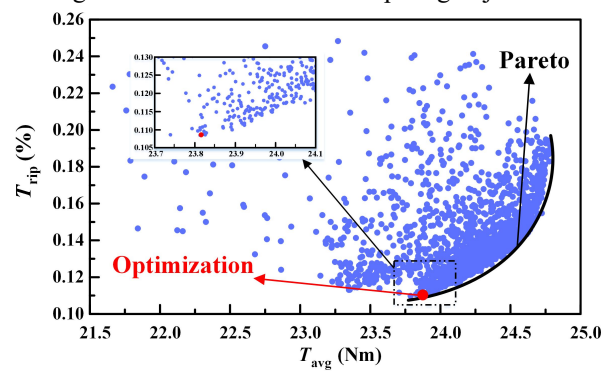


Fig. 8. MOGA-II optimization results.

## D. Optimization results

TABLE IV
COMPARISON OF DIMENSIONS BEFORE AND AFTER

Optimization	Before	After
variables	optimization	optimization
D	35.0mm	36.9mm
$L_1$	5.6mm	6.27mm
$L_2$	5.0mm	5.17mm
$L_3$	2.2mm	3.00mm
$L_4$	0.7mm	0.00mm
$H_{ m pm1}$	2.8mm	2.73mm
$H_{ m pm2}$	2.0mm	1.94mm
$H_{ m pm3}$	4.0mm	3.42mm
$W_{ m pm2}$	8.1mm	8.79mm
71	128°	125.5°
$\gamma_2$	133°	136.8°
γ3	168°	168.8°

Comprehensive analysis of the above hierarchical multiobjective optimization results determines the optimized motor scheme. Table IV compares the design variable values before and after optimization, while Table V shows the NdFeB permanent magnet consumption comparison between the optimized motor and TIPMM. Compared with the pre-optimization motor, the NdFeB dosage of the post-optimization motor only increases by 0.025%, however, the torque of the optimized motor reaches 23.81 Nm, compared to 22.57 Nm for the initial design, the torque is increased by 5.49%, while torque ripple is reduced by 19.3%. Furthermore, compared with TIPMM, the optimized motor reduces NdFeB consumption by 15.6%, which significantly lowers production costs.

 $\label{table V} TABLE~V\\ COMPARISON~OF~NdFeB~PERMANENT~MAGNET~USAGE$ 

Motors	NdFeB Consumption
Before optimization motor	36254.40mm <sup>3</sup>
After optimization motor	36263.57mm <sup>3</sup>
TIPMM	42952.00mm <sup>3</sup>

# IV. ELECTROMAGNETIC CHARACTERISTICS ANALYSIS

#### A. No-load back-EMF

The no-load back-EMF waveforms of MAOHP-IPMM and TIPMM are shown in Fig. 9. It can be seen that the MAOHP-IPMM back-EMF amplitude is significantly higher than that of TIPMM, and its waveform exhibits a phase shift relative to the symmetrical case. According to the analysis based on the motor steady-state vector diagram above, this phase shift angle is equal to the magnetic axis offset angle  $\gamma$ .

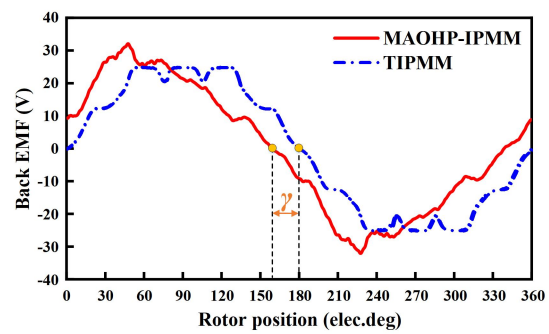


Fig. 9. No-load back-EMF.

## B. Inductance

The comparison of inductance characteristics between MAOHP-IPMM and TIPMM is shown in Fig. 10. Finite element simulation results indicate that the inductance difference  $\Delta L_{\rm dq}$  for MAOHP-IPMM and TIPMM is 149.43  $\mu$ H and 139.08  $\mu$ H, respectively. Compared with TIPMM, the inductance difference of the proposed MAOHP-IPMM increased by 7.4%. According to the reluctance torque expression in Eq. (14), this enhancement confers superior reluctance torque output capability to MAOHP-IPMM.

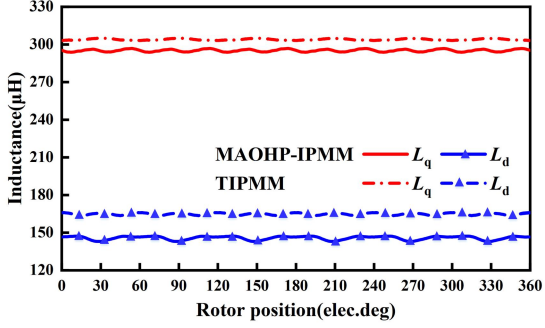


Fig. 10. Inductance characteristic.

## C. Torque-current angle characteristics

Freezing permeability is used to analyze the torquecurrent angle characteristics of MAOHP-IPMM and TIPMM under load conditions, separating the permanent magnet torque and reluctance torque components, as shown in Fig. 11. The maximum permanent magnet torque of MAOHP-IPMM is obtained at 23° current angle, while the maximum permanent magnet torque of TIPMM is obtained at 0° current angle. It is evident that the permanent magnet torque of MAOHP-IPMM is offset to the right, with a magnetic axis offset angle  $\gamma=23^{\circ}$ , which corresponds to the offset angle γ of no-load back-EMF. However, the increased asymmetry in the optimized motor rotor structure also leads to a slight shift in the reluctance torque of the MAOHP-IPMM as well, with its maximum value occurring at 49°. Overall, the difference in the current phase angle between the maximum values of the permanent magnet torque and the reluctance torque components of the MAOHP-IPMM is reduced from the conventional 45° to 26°, leading to a larger total torque.

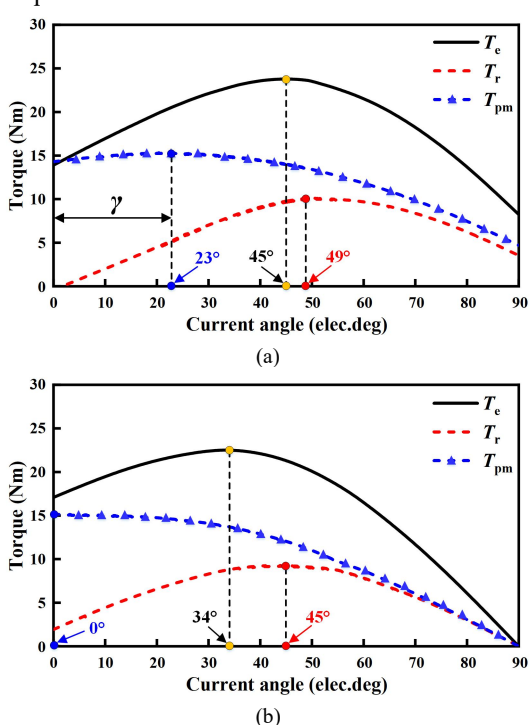


Fig. 11. Torque-current angle characteristics. (a) MAOHP-IPMM. (b) TIPMM.

Define the total torque synthesized when the permanent magnet torque and reluctance torque reach their maximum value at the same current angle as the theoretical maximum torque  $T_{\rm max}$ , thus the torque utilization can be defined as

$$\eta = \frac{T_0}{T_{\text{max}}} \tag{19}$$

where  $\eta$  is the torque utilization of the motor, and  $T_0$  is the actual total torque.

According to Eq. (19), the torque utilization of the MAOHP-IPMM and TIPMM is calculated to be 93.5% and 91.6%, respectively. Compared to the TIPMM, the torque utilization of MAOHP-IPMM is increased by 2.1%.

## D. Output torque

The output torque of MAOHP-IPMM and TIPMM at the optimum current angles of  $45^{\circ}$  and  $34^{\circ}$  are separated to

obtain the waveforms of the two motors with different torque components, as shown in Fig. 12. It can be clearly seen in the figure that the average torque of MAOHP-IPMM is 23.81 Nm with 10.97% torque ripple, while the average torque of TIPMM is 22.56 Nm with 18.98% torque ripple. Although the amount of NdFeB is reduced by 15.6%, the permanent magnet torque and reluctance torque of MAOHP-IPMM are higher than those of TIPMM, resulting in a 5.5% increase in average torque and a 42.2% reduction in torque ripple compared with TIPMM. In addition, the ripple of both the permanent magnet torque and reluctance torque of the proposed motor is larger than that of TIPMM, but the total torque ripple is much smaller than that of TIPMM. This is due to the MAO characteristic, specifically, the MAO characteristic induces a phase shift between the ripple waveforms of the permanent magnet torque and reluctance torque in the MAOHP-IPMM. As shown in Fig. 12(a), when the permanent magnet torque reaches its peak, the reluctance torque coincides with its valley, forming a complementary cancellation effect. This mechanism significantly reduces the ripple amplitude of the synthesized total torque. In contrast, the torque ripple phases of the two components in the TIPMM are relatively consistent, resulting in larger total torque ripple after superposition. This phenomenon verifies the positive role of the MAO effect in suppressing torque ripple.

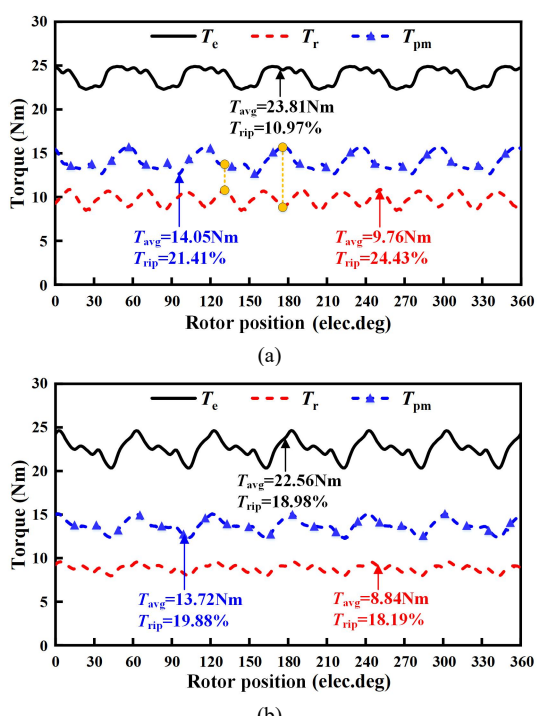


Fig. 12. Torque separation curve. (a) MAOHP-IPMM. (b) TIPMM.

## E. Speed - torque and power curves

The relationship curves between output torque-speed and output power-speed for MAOHP-IPMM and TIPMM under rated operating conditions are shown in Fig. 13. In the constant torque region within 3000 r/min, MAOHP-IPMM demonstrates higher output torque than TIPMM, showing obvious torque enhancement effects. In the low-speed constant power region, MAOHP-IPMM delivers higher output power than TIPMM, with maximum output power of 8.68 kW and 8.51 kW, respectively. When the rotational

speed exceeds 7000 r/min, the output performance of both machines begin to deteriorate, and the output torque and power of MAOHP-IPMM are lower than those of TIPMM. This is mainly because its higher permanent magnet flux linkage leads to an increase in back EMF when the motor operates at high speeds. To maintain high-speed operation, the motor needs to pass a stronger flux-weakening current to weaken the flux linkage, which consequently results in a certain decrease in the motor's output torque and power.

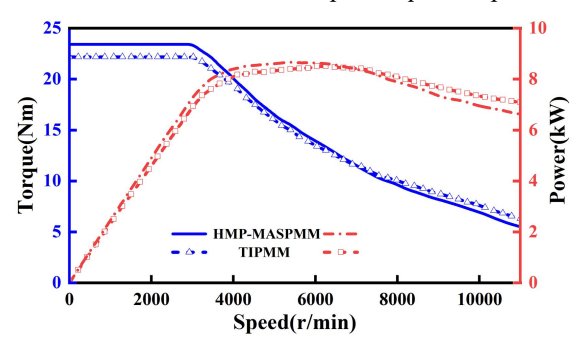


Fig. 13. Speed-torque and power curves.

# F. Efficiency

Fig. 14 shows the efficiency map of the two motors under rated operating conditions, with both motors controlled using MTPA and flux-weakening strategies. It can be seen that the efficiency distribution is similar for both motors, each reaching a maximum efficiency of 95%. However, the high efficiency region where efficiency exceeds 95% is significantly larger for MAOHP-IPMM than that of TIPMM.

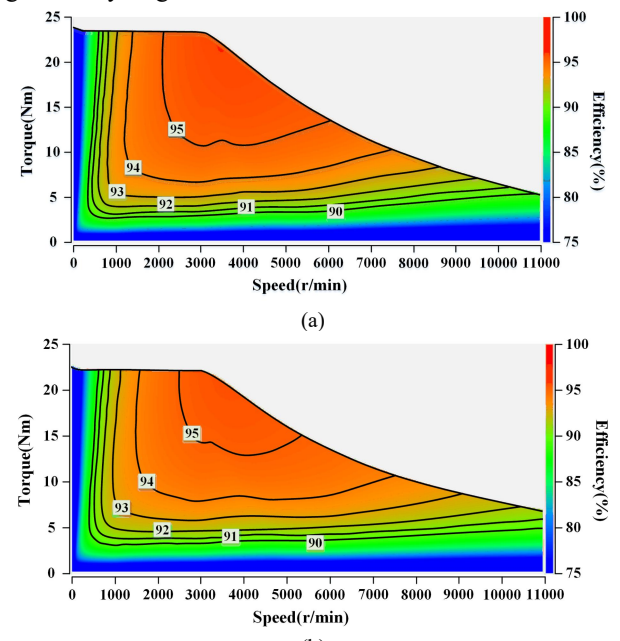


Fig. 14. Efficiency map. (a) MAOHP-IPMM. (b) TIPMM.

# V. EXPERIMENTAL VERIFICATION

In order to verify the correctness of theoretical analysis and finite element analysis, a prototype of MAOHP-IPMM is fabricated based on the optimized motor parameters, and relevant experiments are carried out. The structure of the prototype is shown in Fig. 15.

The motor no-load test platform is shown in Fig. 16, including servo motor and its control platform, prototype

under test, oscilloscope and LCR tester. No-load back-EMF test is carried out firstly, the prototype under test is connected to the servo motor and the servo motor is controlled by the servo motor controller to drag the prototype to rotate. The three-phase wires of the prototype under test are connected to the three signal wires of the oscilloscope.



Fig. 15. Experimental prototype. (a) Stator. (b) Permanent magnets and silicon steel sheets. (c) Rotor.

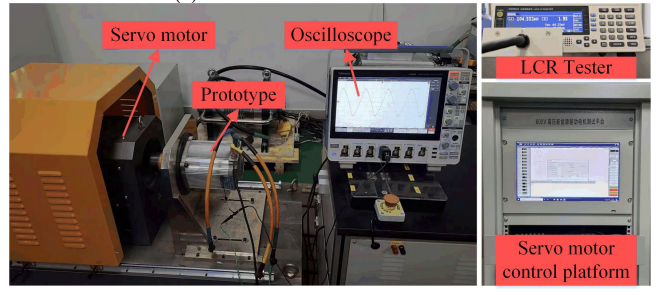


Fig. 16. Motor no-load experiment platform.

When the rotational speed stabilized at 3000 r/min, the no-load back-EMF waveform of the motor is measured, as shown in Fig. 17. Fig. 17(a) presents the experimentally measured three-phase back-EMF waveform, while Fig. 17(b) shows the comparison between the experimental and FEA back-EMF waveforms. The observed difference in the waveforms is mainly attributable to manufacturing errors and the neglect of the winding end effects in the finite element simulation process.

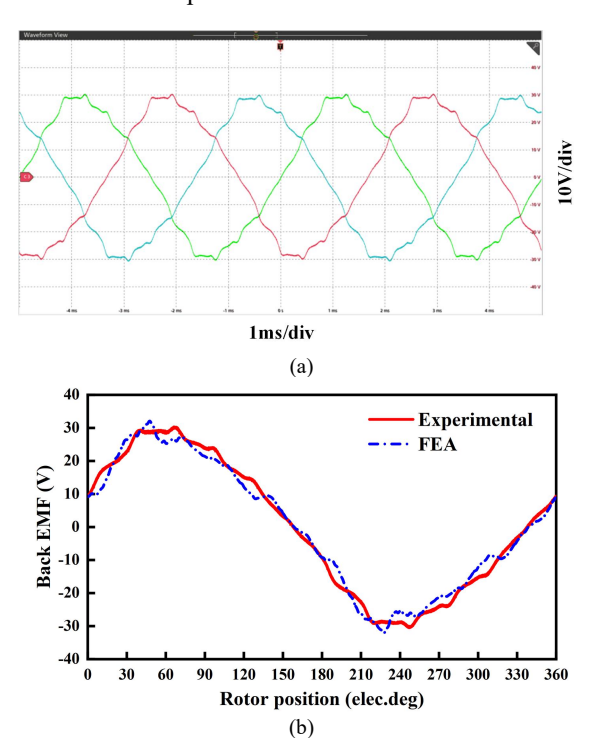


Fig. 17. No-load back-EMF. (a) Measured three-phase back-EMF waveforms. (b) Comparison of experimental and FEA.

To verify the inductance characteristics of the MAOHP-IPMM, the LCR tester is used to measure the three-phase

inductance values of the prototype under the no-load condition. The dq-axis inductance comparison of the experimental and FEA results is presented after coordinate transformation, as shown in Fig. 18. Due to processing errors, the average value of the dq-axis inductance obtained from the experiment is slightly smaller than the FEA result. However, the inductance difference  $\Delta L_{\rm dq}$  measured experimentally is 149.12  $\mu$ H, close to the FEA result.

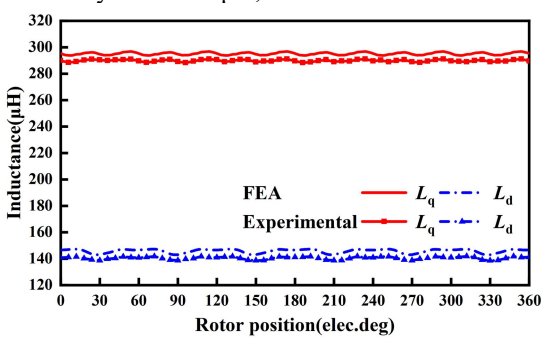


Fig. 18. Comparison of inductance waveforms between experiment and FF  $\Delta$ 

The motor load experiment platform is shown in Fig. 19. In this setup, the servo motor is connected to the prototype under test, and load torque is applied to the prototype. Control commands are sent to the controller via the upper computer to control the motor rotation. Subsequently, the motor load characteristics are analyzed by the power analyzer.

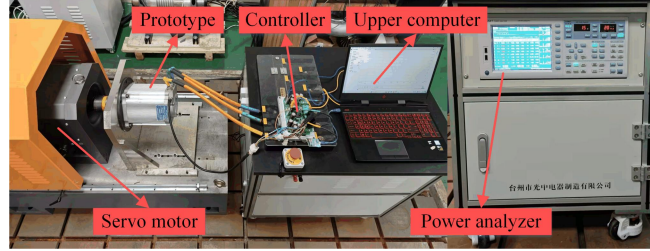


Fig. 19. Motor load experiment platform.

To verify the MAO characteristics of the MAOHP-IPMM, the torque-current angle characteristics of the prototype are measured. Values are recorded at intervals of 10° current angle, and the results are shown in Fig. 20. It can be found that the torque-current angle curve obtained by the experiment is closely matches the FEA results, and the maximum torque occurs at approximately 45° current angle.

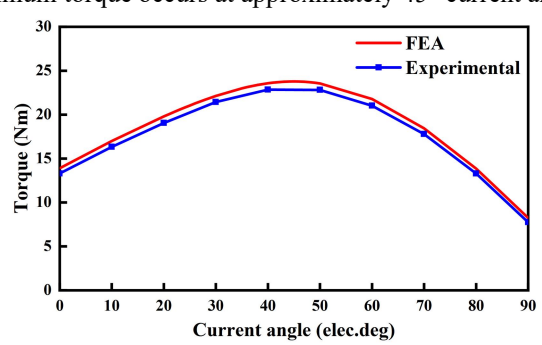


Fig. 20. Comparison of experimental and FEA torque-current angle characteristics.

## VI. CONCLUSION

In this paper, a novel MAOHP-IPMM is proposed. Owing to the asymmetric permanent magnet and barrier arrangement, the MAOHP-IPMM achieves the MAO effect,

which reduce the current angle difference between the maximum permanent magnet torque and the maximum reluctance torque, and improve the motor's torque utilization. Based on the traditional mathematical model of permanent magnet motor, the magnetic axis offset angle  $\gamma$  is introduced, establishing the mathematical model of the MAOHP-IPMM from the perspective of power balance. This model guides the structure optimization and analysis. Additionally, the output torque and torque ripple are optimized by using a hierarchical multi-objective optimization method. comparison of the electromagnetic characteristics between the MAOHP-IPMM and the TIPMM shows that the inductance difference of the MAOHP-IPMM is 7.4% higher than that of the TIPMM, the current angle difference between the maximum permanent magnet torque and reluctance torque has been reduced from the conventional 45° to 26°, and the average torque has been improved by 5.5%, while the amount of NdFeB permanent magnets has been reduced by 15.6% and the torque ripple is reduced by 42.2%. These improvements further reduce the consumption of rare-earth permanent magnet materials and improve the torque utilization.

## REFERENCES

- S. Zheng, X. Zhu, L. Xu, Z. Xiang, L. Quan and B. Yu, "Multi-Objective Optimization Design of a Multi-Permanent-Magnet Motor Considering Magnet Characteristic Variation Effects," in IEEE Transactions on Industrial Electronics, vol. 69, no. 4, pp. 3428-3438, April 2022.
- [2] X. Xie, C. Liao and Z. Zhang, "Design Considerations of High-Speed PMSM With Nonuniform Two-Segment Halbach Magnet Array," in IEEE Transactions on Magnetics, vol. 60, no. 9, pp. 1-6, Sept. 2024.
- [3] L. Shi, J. Jing, W. Wang, Z. Liu and F. Li, "Electromagnetic Characteristic Analysis of a Negative-Salient Hybrid Permanent Magnet Motor for Electric Vehicles," in IEEE Journal of Emerging and Selected Topics in Industrial Electronics, vol. 5, no. 3, pp. 1283-1291, July. 2024.
- [4] F. Mahmouditabar, A. Vahedi and N. Takorabet, "Design and Analysis of Interior Permanent Magnet Motor for Electric Vehicle Application Considering Irreversible Demagnetization," in IEEE Transactions on Industry Applications, vol. 58, no. 1, pp. 284-293, Jan.-Feb. 2022.
- [5] X. Zhu, and Y. Yan, "Study on Winding Inductances in Stator Surface-Mounted Permanent Magnet Machines," Energies, vol. 15, no. 21, pp. 53-259, Oct. 2024.
- [6] T. -A. Huynh, Y. -T. Nguyen Le, Z. Lee, M. -C. Tsai, P. -W. Huang and M. -F. Hsieh, "Influence of Flux Barriers and Permanent Magnet Arrangements on Performance of High-Speed Flux-Intensifying IPM Motor," in IEEE Transactions on Magnetics, vol. 59, no. 11, pp. 1-6, Nov. 2023.
- [7] S. Zheng, X. Zhu, L. Xu, T. Zhu and D. Wu, "Comparative Analysis and Multi-Objective Optimization of Hybrid Permanent Magnet Motors Considering Different Saliency Characteristics," in IEEE Transactions on Applied Superconductivity, vol. 31, no. 8, pp. 1-5, Nov. 2021.
- [8] J. Ou, Y. Liu and M. Doppelbauer, "Comparison Study of a Surface-Mounted PM Rotor and an Interior PM Rotor Made From Amorphous Metal of High-Speed Motors," in IEEE Transactions on Industrial Electronics, vol. 68, no. 10, pp. 9148-9159, Oct. 2021.
- [9] K. Liu, L. Shi, Z. Liu, et al, "Analysis and Optimization of Asymmetric Hybrid Permanent Magnet Motor for Electric Vehicle," Journal of Electrical Engineering & Technology, vol. 18, no. 5, pp. 3355-3567, Sept. 2023.
- [10] C. Diao, W. Zhao, Y. Liu and X. Wang, "Permanent Magnet Assisted Synchronous Reluctance Motor with Asymmetric Rotor for High Torque Performance," in CES Transactions on Electrical Machines and Systems, vol. 7, no. 2, pp. 179-186, June 2023.
- [11] A. Mohammadi and S. M. Mirimani, "Design of a Novel PM-Assisted Synchronous Reluctance Motor Topology Using V-Shape Permanent Magnets for Improvement of Torque Characteristic," in IEEE

- Transactions on Energy Conversion, vol. 37, no. 1, pp. 424-432, March 2022.
- [12] B. Poudel, E. Amiri, P. Rastgoufard and B. Mirafzal, "Toward Less Rare-Earth Permanent Magnet in Electric Machines: A Review," in IEEE Transactions on Magnetics, vol. 57, no. 9, pp. 1-19, Sept. 2021.
- [13] D. Xiao, L. Shi, F. Li, S. Gao and X. Tao, "Electromagnetic Characteristics Study of Segmental Rotor Dual Mode Reluctance Starter Generator," in *IEEE Transactions on Transportation Electrification*, vol. 11, no. 1, pp. 204-214, Feb. 2025.
- [14] J. -X. Shen, Y. -Q. Lin, Y. Sun, X. -F. Qin, W. -J. Wan and S. Cai, "Permanent Magnet Synchronous Reluctance Machines With Axially Combined Rotor Structure," in IEEE Transactions on Magnetics, vol. 58, no. 2, pp. 1-10, Feb. 2022.
- [15] Z. Liu, Y. Hu, J. Wu, B. Zhang and G. Feng, "A Novel Modular Permanent Magnet-Assisted Synchronous Reluctance Motor," in IEEE Access, vol. 9, pp. 19947-19959, 2021.
- [16] G. Xu, G. Liu, W. Zhao, Q. Chen and X. Du, "Principle of Torque-Angle Approaching in a Hybrid Rotor Permanent-Magnet Motor," in IEEE Transactions on Industrial Electronics, vol. 66, no. 4, pp. 2580-2591, April 2019.
- [17] Y. Xie, J. Shao, S. He, B. Ye, F. Yang and L. Wang, "Novel PM-Assisted Synchronous Reluctance Machines Using Asymmetrical Rotor Configuration," in IEEE Access, vol. 10, pp. 79564-79573, 2022
- [18] Y. Xiao, Z. Q. Zhu, G. W. Jewell, J. T. Chen, D. Wu and L. M. Gong, "A Novel Asymmetric Interior Permanent Magnet Synchronous Machine," in IEEE Transactions on Industry Applications, vol. 58, no. 3, pp. 3370-3382, May.-June 2022.
- [19] A. Nobahari, A. Vahedi and R. Nasiri-Zarandi, "A Modified Permanent Magnet-Assisted Synchronous Reluctance Motor Design for Torque Characteristics Improvement," in IEEE Transactions on Energy Conversion, vol. 37, no. 2, pp. 989-998, June 2022.
- [20] Y. Lu, H. Yang, S. Sazzad, D. Liu, X. Guo and W. Zhang, "Investigation of Novel Interior PM Machine with Asymmetric Magnet Distributions for EV Application," 2023 IEEE 6th International Electrical and Energy Conference (CIEEC), Hefei, China, 2023, pp. 4572-4577.
- [21] Y. Xiao, Z. Q. Zhu, J. T. Chen, D. Wu and L. M. Gong, "A Novel V-shape Interior Permanent Magnet Synchronous Machine with Asymmetric Spoke-type Flux Barrier," 2020 International Conference on Electrical Machines (ICEM), Gothenburg, Sweden, 2020, pp. 382-388.
- [22] Y. Xiao, Z. Q. Zhu, G. W. Jewell, J. Chen, D. Wu and L. Gong, "A Novel Spoke-Type Asymmetric Rotor Interior Permanent Magnet Machine," in IEEE Transactions on Industry Applications, vol. 57, no. 5, pp. 4840-4851, Sept.-Oct. 2021.